

Comparing heterogeneity of sea ice models with Viscous-Plastic and Maxwell Elasto-Brittle rheology

Mirjam BOURGETT¹, Martin LOSCH¹, Mathieu PLANTE²

¹*Alfred-Wegener-Institut für Polar- und Meeresforschung, Bremerhaven, Germany*

²*Recherche en prévision numérique environnementale, Environnement et Changement Climatique
Canada, Dorval, Québec, Canada*

Correspondence: Mirjam Bourgett <mirjam.bourgett@awi.de>

ABSTRACT.

Classical sea-ice models in climate model resolution do not resolve the small scale physics of sea ice. New methods to address this problem include modifications to established viscous-plastic (VP) rheology models, sub-grid scale parameterisations, or new rheologies such as the Maxwell elasto-brittle (MEB) rheology. Here, we investigate differences in grid-scale dynamics simulated by the VP and MEB models, their dependency on tunable model parameters and their response to added stochastic perturbations of material parameters in a new implementation in the Massachusetts Institute of Technology general circulation model. Idealized simulations are used to demonstrate that material parameters can be tuned so that both VP and MEB rheologies lead to similar cohesive stress states, arching behavior, and heterogeneity in the deformation fields. As expected, simulations with MEB rheology generally show more heterogeneity than the VP model as measured by the number of simulated linear kinematic features (LKFs). For both rheologies, the cohesion determines the emergence of LKFs. Introducing grid-scale heterogeneity by random model parameter perturbation, however, leads to a larger increase of LKF numbers in the VP simulations than in the MEB simulations and similar heterogeneity between VP and MEB models.

This is an Open Access article, distributed under the terms of the Creative Commons Attribution NonCommercial-NoDerivatives licence (<http://creativecommons.org/licenses/by-nc-nd/4.0/>), which permits non-commercial re-use, distribution, and reproduction in any medium, provided the original work is unaltered and is properly cited. The written permission of Cambridge University Press must be obtained for commercial re-use or in order to create a derivative work.

27 **INTRODUCTION**

28 Representing sea ice deformations in large scale climate models is important but challenging as the large
29 scale sea ice conditions very much depend on smaller-scale physics that are poorly resolved at coarse resolu-
30 tion. Most continuum sea ice models use the viscous-plastic (VP) rheology (Hibler, 1979) or modifications
31 (e.g. the Elastic Viscous Plastic or EVP, Hunke and Dukowicz, 1997), which has been used for decades to
32 reproduce the observed sea ice thickness, concentration and velocity fields. At high resolution, VP models
33 are able to reproduce some of the large scale statistics of sea ice deformations, for instance the observed
34 multi-fractal spatial and temporal scaling (Hutter and Losch, 2020; Bouchat and others, 2022; Hutter and
35 others, 2022). At coarser resolutions, however, the scaling properties of sea ice deformations from VP
36 models can be inconsistent with observations (Weiss and others, 2007; Bouchat and others, 2022; Hutter
37 and others, 2022). In particular, models using the VP rheology tend to underestimate intermittency and
38 spatial heterogeneity because they cannot trigger multi-scale deformation events from smaller scale per-
39 turbations (Weiss and others, 2007). At grid resolutions of ≈ 12 km, the VP rheology did not reproduce
40 the complicated fracturing processes associated with sea ice deformations and their organisation into a
41 network of localised lines with large deformations called Linear Kinematic Features (LKFs) (Girard and
42 others, 2011).

43 This challenge sparked different approaches to include smaller scale characteristics in large scale models.
44 To allow for fine scale features, existing VP models were modified to use different yield curves (Ringeyen
45 and others, 2019, 2023), flow rules (Ringeyen and others, 2021), grids (Danilov and others, 2017; Turner
46 and others, 2022; Rampal and others, 2016) and numerical methods (Lemieux and others, 2008, 2010; Losch
47 and others, 2014). Alternatively, new rheologies were suggested that include sub-grid parameterisations
48 to better represent fracture physics. In particular, brittle (elasto-brittle or EB, Maxwell elasto-brittle
49 or MEB, brittle Bingham-Maxwell or BBM) rheologies (Girard and others, 2011; Dansereau and others,
50 2016; Ólason and others, 2022) introduced a damage parameter that represents the presence of sub-grid
51 scale fractures, allowing for (and keeping a memory of) material property degradation under high stresses
52 without large deformations. These still relatively new brittle rheologies simulate realistic large scale fields
53 with adequate heterogeneity and intermittency even at coarser resolution (grid spacing of ≈ 10 km) (e.g.
54 Ólason and others, 2022). Another way of accounting for the missing physical sub-grid scale processes
55 is to use stochastic parameterizations (e.g. Juricke and others, 2013) where the effect of unresolved small

56 scales on the large scales are not modeled in a deterministic way from the resolved flow, but by randomly
57 perturbing selected model parameters (Berner and others, 2017). This method has also been used with
58 brittle rheologies in idealized experiments (Girard and others, 2011; Dansereau and others, 2016).

59 As part of their development, new rheology parameterizations are often evaluated in idealised experi-
60 ments that are designed to test, tune, and compare the model to observed sea ice dynamical behaviour. For
61 instance, ideal ice bridge experiments have been used with both the (E)VP (e.g., Dumont and others, 2009;
62 Losch and Danilov, 2012) and MEB (e.g., Dansereau and others, 2017; Plante and others, 2020) rheologies
63 to demonstrate their ability to reproduce the observed tendency for sea ice flow to become obstructed by
64 the formation of self-supporting ice arches in narrow channels (Walker, 1966; Sodhi, 1977). Uniaxial com-
65 pression experiments have been used to assess the influence of the plastic flow rules on the orientation of
66 LKFs in VP models (Ringeyen and others, 2019, 2021, 2023). A benchmark experiment was also designed
67 to assess the LKFs and heterogeneity in the sea ice cover under convergent or divergent wind forcing. This
68 benchmark experiment proved useful to formulate metrics and compare LKFs statistics from different sea
69 ice models (Mehlmann and others, 2021; Hutter and Losch, 2020).

70 Often a given sea ice model code implements only one type of rheology. This leads to rheology compar-
71 isons that are confounded by numerical discretization, advection scheme, and grid resolution (Bouchat and
72 others, 2022; Hutter and others, 2022). Sea ice model codes that contain more than one rheology are, for
73 example, the McGill sea ice model (Plante and others, 2020) or the neXtSIM (Ólason and others, 2022).
74 The McGill model contains the MEB and an implicit VP rheology with different solution techniques, but
75 is not coupled to an ocean (Plante and others, 2020). The neXtSIM framework, for which coupled set-ups
76 exist, is a Lagrangian sea ice model and implements MEB, BBM, and m(odified)EVP rheology (Ólason
77 and others, 2022; Boutin and others, 2023). Here, we add the MEB rheology to the sea ice component
78 (Losch and others, 2010) of the open source Massachusetts Institute of Technology general circulation
79 model (MITgcm, Marshall and others, 1997; MITgcm Group, 2021). The sea ice component already con-
80 tains VP rheologies with many different options and yield curves (Losch and others, 2010, 2014; Kimmritz
81 and others, 2016; Ringeyen and others, 2023; MITgcm Group, 2021) for the purpose of unconfounded
82 comparisons between sea ice rheologies in a coupled ice ocean framework.

83 In this paper, we investigate the sea ice deformations and heterogeneity simulated by the VP and MEB
84 rheologies in the context of ideal ice bridge and benchmark experiments. To do so, the MEB rheology
85 is implemented in the MITgcm sea ice component as to provide an unconfounded comparison framework.

86 The MEB implementation follows and is validated against Plante and others (2020). A similar ice bridge
87 experiment is then used to compare deformation features of simulations with MEB and VP rheology. The
88 spatial heterogeneity simulated with both rheologies is then evaluated in an idealized quadratic domain with
89 cyclonic winds (Mehlmann and others, 2021) by tracking LKFs. To further increase spatial heterogeneity
90 with both VP and MEB rheologies a stochastic parameterisation is presented.

91 MODEL DESCRIPTION

92 The MITgcm is a general circulation model used to study atmosphere, ocean, and climate processes at
93 all scales (Marshall and others, 1997; MITgcm Group, 2021). It employs a finite volume discretization on
94 an Arakawa C-grid. The sea ice model is coupled to the ocean and implements the VP rheology (Hibler,
95 1979) with a number of yield curves and solvers (e.g., Losch and others, 2010, 2014; Kimmritz and others,
96 2016; Ringeisen and others, 2023; MITgcm Group, 2021). The MITgcm model code and documentation
97 can be found at <https://mitgcm.org>. This paper addresses the dynamics of the sea ice model and all
98 thermodynamics processes are turned off.

99 MEB constitutive equation

100 The MEB rheology consists of a linear elastic part of the constitutive equation for a continuous solid,
101 a viscous part of the constitutive equation for irreversible deformations, a local Mohr Coulomb (MC)
102 criterion for brittle failure, and an isotropic progressive damage mechanism that rescales the viscous and
103 elastic dynamics to initiate avalanches of damage (Dansereau and others, 2016). We repeat the main
104 aspects here for clarity.

105 The constitutive equation for vertically integrated internal stress $\boldsymbol{\sigma}$ (here in Pa m = N m⁻¹) and strain
106 rates $\dot{\boldsymbol{\epsilon}}$ for a 2D compressible, visco-elastic, continuous solid is

$$\dot{\boldsymbol{\sigma}} + \lambda^{-1}\boldsymbol{\sigma} = E(d)\boldsymbol{C} \cdot \dot{\boldsymbol{\epsilon}} \quad (1)$$

107 with the elastic modulus tensor \boldsymbol{C} (a function of the Poisson ratio ν) and the viscous relaxation time scale
108 λ . Note that the stress and strain rate tensors are reduced in their order by using the Voigt notation
109 for symmetric tensors. The relaxation time scale λ is written as the ratio of the viscosity ξ , the elastic
110 modulus E , and a damage parameter d representing the amount material degradation from accumulating

111 micro (sub-grid) cracks in the sea ice (Dansereau and others, 2016):

$$\lambda = \frac{\xi(d)}{E(d)} = \lambda_0 (1 - d)^{\alpha-1} \quad (2)$$

112 where ξ and E depend on the fractional ice cover, mean ice thickness (i.e., using the formulation for the
113 VP ice strength of Hibler, 1979) and $\alpha > 1$ is a parameter ruling the transition from elastic to viscous
114 behaviour. E_0 and ξ_0 are the undamaged mechanical parameters and $\lambda_0 = \frac{\xi_0}{E_0}$. In contrast to some previous
115 work (e.g., Dansereau and others, 2016), we define damage so that $d = 0$ for undamaged ice and $d = 1$ for
116 maximally damaged ice.

117 The damage increases when the stress states exceed the yield curve (Fig. 1) and it contains the history
118 of the previous damaging events (Dansereau and others, 2016; Plante and others, 2020). The increase
119 depends on the scaling factor d_{crit} (critical damage, which is determined by the requirement to bring the
120 overshooting stress state back to the yield curve).

121 One possible yield curve for the MEB rheology is the MC criterion with a tensile cut-off (Fig. 1)
122 (Dansereau and others, 2016). The critical uniaxial compressive stress σ_c at the intersection of the MC
123 yield curve with the principal stress σ_1 axis (Fig. 1) is

$$\sigma_c = 2ch\sqrt{q} \quad (3)$$

124 where c is the cohesion and $q = \left((\mu^2 + 1)^{1/2} + \mu\right)^2$ is the slope defined by the internal friction coefficient
125 μ . In contrast to the standard elliptic yield curve of a VP rheology (Hibler, 1979), this yield curve permits
126 isotropic tensile stresses. The critical tensile stress σ_t is defined as the intersection of the principal stress
127 σ_2 axis with the MC criterion (Fig. 1) so that

$$\sigma_t = -\frac{\sigma_c}{q}. \quad (4)$$

128 Implementation details

129 The finite-volume implementation on the C-grid of the MITgcm sea ice model follows for the most part
130 the implementation of the MEB rheology in the finite-differences C-grid implementation in the McGill sea
131 ice model (Plante and others, 2020).

132 We note the structural similarity of the MEB and VP constitutive equations: the product of the elastic

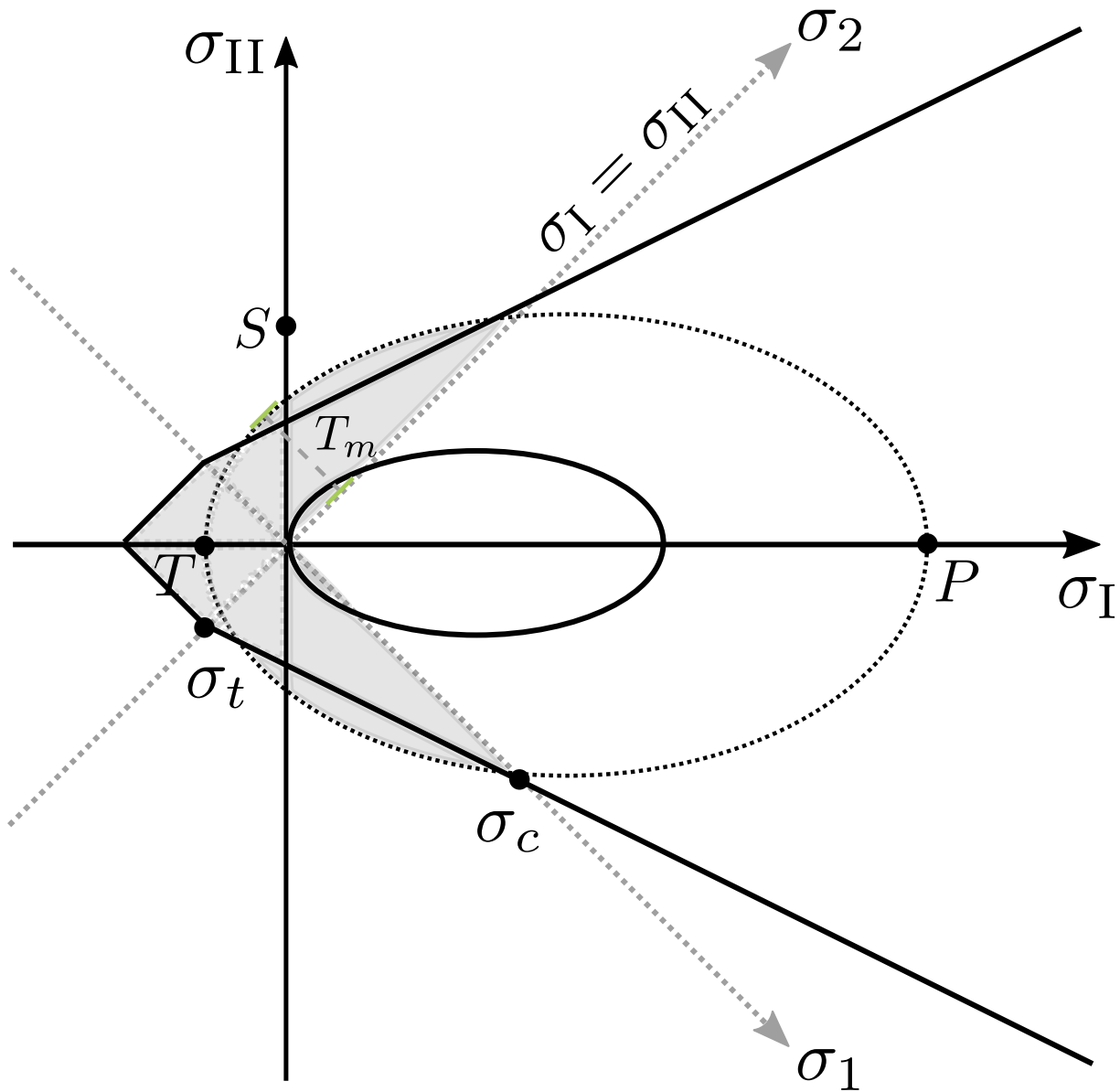


Fig. 1. Illustration of elliptic yield curve (VP, black dotted and solid ellipses) and Mohr-Coulomb yield curve (MEB, black piecewise linear lines). Invariant stress axes (σ_I , σ_{II}) in black and principal stress axes (σ_1 , σ_2) in grey. σ_c is the critical uniaxial compressive stress (Eq. 3) and σ_t is the critical tensile stress (Eq. 4). The maximum tensile stress T_m (Eq. 6) is indicated by the green dashed line. a and b denote the semi-major axes of the elliptic yield curve. Grey shading marks the cohesive stress states.

133 modulus tensor \mathbf{C} and the strain rate tensor $\dot{\boldsymbol{\epsilon}}$ in (1) is (e.g., Dansereau and others, 2016)

$$[\mathbf{C} \cdot \dot{\boldsymbol{\epsilon}}^n]_{ij} = \frac{\nu}{(1+\nu)(1-\nu)} \dot{\epsilon}_{kk} \delta_{ij} + \frac{1}{1+\nu} \dot{\epsilon}_{ij}. \quad (5)$$

134 This is the same form as the VP constitutive equation $\sigma_{ij} = 2\eta\dot{\epsilon}_{ij} + \left[(\zeta - \eta)\dot{\epsilon}_{kk} - \frac{P}{2} \right] \delta_{ij}$ with $P = 0$ and
 135 shear and bulk viscosities $\eta = \frac{1}{2} \frac{1}{1+\nu}$ and $\zeta = \frac{1}{2} \frac{1}{1-\nu}$. After re-interpreting these variables, we can re-use
 136 most of the VP-code without additional changes. For details of the discretisation we refer to Plante and
 137 others (2020).

138 On the staggered C-grid, some variables are naturally defined at center (C) points (e.g., σ_{11}), while
 139 others are naturally defined at corner (Z) points (e.g., σ_{12} and $\dot{\epsilon}_{12}$) (Losch and others, 2010). Numerical
 140 stability requires that σ_{12} , d_{crit} , d , λ^{-1} , and E are defined on both C- and Z-points of the C-grid cell. The
 141 associated averaging is reduced to a minimum, so that only d_{crit} , d , h , a are linearly averaged to Z-points
 142 and only $(\dot{\epsilon}_{12})^2$ is averaged to C-points. E , λ^{-1} , and σ_{12} are computed for center and corner points with
 143 the averaged variables.

144 Validation

145 We confirmed the plausibility of our MEB implementation with analytic solutions and symmetry tests (not
 146 shown, see Chapters 6 and 7 in Bourgett, 2022) and with a reproduction of an idealized ice channel (Plante
 147 and others, 2020, not shown).

148 The general behaviour of the dynamics is identical to previous results (Plante and others, 2020). At the
 149 beginning of the simulation the tensile stresses downstream of the channel increase and damage develops
 150 downstream of each channel boundary. After 3300 s ($\tau = 0.06 \text{ N m}^{-2}$) a concave shape at the downstream
 151 end of the channel indicates the ice arching effect. The stress values agree with the previous results (Plante
 152 and others, 2020, their Fig. 9). The divergent stress in the middle of the channel is small. The tensile
 153 stresses and the shear stresses in the downstream corners of the channel increase so that damage extends
 154 over the channel. The ice detaches from the upstream coastline but does not move yet (it remains landfast,
 155 land-locked by the islands). Both shear and divergent stress fields downstream of the ice channel drop to
 156 zero when the ice downstream of the channel detaches (not shown, see Chapter 7 in Bourgett, 2022).

Table 1. Model parameters of the channel with idealised ice bridge experiment and the quadratic domain with cyclonic winds (“benchmark”) for the MEB and the VP rheology.

Parameter	Definition	channel		“benchmark”		Unit
		MEB	VP	MEB	VP	
Δx	Spatial resolution	2		2, 4, 8		km
Δt	Time step	0.5		0.5	120	s
T_d	Damage time	2	-	2	-	s
T_h	Healing time	-	-	1×10^5	-	s
E_0	Elastic modulus	1×10^9	-	5×10^8	-	N m^{-2}
P^*	Ice strength	-	27.5	-	27.5	kN m^{-2}
ν	Poisson ratio	0.3	-	0.3	-	
λ_0	Relaxation time scale	1×10^5	-	1×10^7	-	s
α	Damage parameter	4	-	4	-	
μ	Internal friction	0.71	-	0.7	-	
c	Cohesion	10, 30, 50	-	1.56, 25	-	kN m^{-2}
e	Ellipse aspect ratio	-	1.2, 1.6, 2	-	2	
ρ_a	Air density	1.3		1.3		m^{-3}
ρ_i	Sea ice density	9×10^2		9×10^2		m^{-3}
ρ_w	Water density	1.026×10^3		1.026×10^3		m^{-3}
C_a	Air drag coefficient	1.2×10^{-3}		1.2×10^{-3}		
C_w	Water drag coefficient	5.5×10^{-3}		5.5×10^{-3}		
f_0	Coriolis parameter	0		1.46×10^{-4}		s^{-1}
C^*	Ice concentration parameter	20		20		

157 COMPARISON OF MEB TO VP

158 We can now use the MITgcm model framework to compare small-scale sea ice deformations with the VP
159 and the MEB rheology using the same grid spacing, discretization, and parameters.

160 For both rheologies the yield curve determines the cohesive strength. The cohesive strength influences
161 the shear deformation of sea ice. If sea ice is driven through a narrow channel the cohesive strength controls
162 the potential for modelled sea ice to form ice arches (Ip, 1993; Hibler and others, 2006; Plante and others,
163 2020).

164 For the VP and the MEB rheology, cohesive stress states $\sigma_I < |\sigma_{II}|$ are marked by grey shading in
165 Fig. 1. In terms of the mechanical strength parameters for maximal compression, shear and isotropic
166 tension (P, S, T), the ellipse aspect ratio is defined as $e = (P + T)/(2S)$ with $T = kP$ and the tensile
167 factor k (Bouchat and Tremblay, 2017; König Beatty and Holland, 2010). For the elliptic yield curve, the
168 cohesion increases by decreasing the ratio e of the two semi-major axes (making the ellipse “fatter”), by
169 increasing P , and by moving or extending the ellipse into the tensile half-plane ($k > 0$). Even though the
170 original VP yield curve does not allow isotropic tensile stresses ($T = 0$ or $k = 0$, black ellipse in Fig. 1), the
171 tensile strength is not zero. The maximum tensile stress, that is the maximal distance of the yield curve
172 to the diagonal $\sigma_I = \sigma_{II}$ or maximum of σ_1 (Bouchat and Tremblay, 2017, and Fig. 1), is defined as

$$T_m = \frac{1}{2} \left\{ (1 + k) \sqrt{1 + e^{-2}} - (1 - k) \right\} P \quad (6)$$

173 and is non-zero for all $k \geq 0$ (Fig. 1).

174 We use an idealized ice channel to tune yield curve parameters of both rheologies to give similar results.
175 Building on this experience, we analyse the effect of grid-scale heterogeneity on the solution in a quadratic
176 domain with cyclonic winds (Mehmann and others, 2021) with similar cohesion for VP and MEB. The
177 VP models uses a JFNK solver that converges with a relative precision of 10^{-4} . All model parameters are
178 summarized in Tabel 1.

179 Channel with idealised ice bridge

180 Inspired by previous ice arch simulations (Dumont and others, 2009; Dansereau and others, 2017), we
181 use an idealized channel set-up modified from Plante and others (2020). A 800 km by 200 km domain
182 with a grid resolution of 2 km and closed boundaries with a no-slip boundary condition in the x -direction

183 features a channel in the y -direction. The channel itself is 200 km long and 60 km wide. The domain has
184 open boundaries at $y = 0$ km and $y = 800$ km with Neumann conditions for all variables. The Neumann
185 conditions ensure that sea ice can drift freely into and out of the domain and does not need to detach from
186 a solid boundary at $y = 800$ km, so that slowing down of the ice upstream the channel is solely determined
187 by the ice arching. The sea ice cover is forced by surface stress in the negative y -direction (“southwards”)
188 that increases linearly from 0 to 0.625 N m^{-2} within 10 h. The simulation is run for 240 h with no further
189 increase of the forcing. The slowing down of the sea ice upstream of the channel due to the formation of
190 ice arches is used for comparison between VP and MEB.

191 Different parameters of the yield curves were tested to allow cohesive stress states. We choose the
192 parameters so that the maximum tensile stress T_m (6) of the VP rheology is equal to the critical tensile
193 stress σ_t (4) of the MEB rheology, since both represent the maximum positive value of the principal
194 stress σ_1 (Fig. 1). Specifically, we choose $c = 10 \text{ kN m}^{-2}$ and 30 kN m^{-2} leading to $\sigma_t = 10.4 \text{ kN m}^{-1}$
195 and 31.24 kN m^{-1} for MEB. The corresponding T_m are computed with $P^* = 49.92 \text{ kN m}^{-2}$ and $P^* =$
196 149.92 kN m^{-2} , $k = 0.05$, and a small value for $e = 1.2$ (Kubat and others, 2006; Lemieux and others,
197 2016).

198 Except for the VP simulations with $T_m = 31.24 \text{ kN m}^{-1}$, the effect of ice arching to the upstream ice
199 drift velocities can be observed and the ice slows down for both VP and MEB simulation (Fig. 2). The
200 parameter set with $T_m = 31.24 \text{ kN m}^{-1}$ makes the ice so stiff that it does not start to move at all. The
201 ice drift in the MEB simulation with $c = 30 \text{ kN m}^{-2}$ decreases within 40 h. For 10 kN m^{-2} , the ice drift
202 upstream increases quickly and then slows down gradually with rates that are very similar between the
203 MEB ($m_{\text{meb}} = 1.45 \times 10^{-7} \text{ m s}^{-2}$) and VP simulations ($m_{\text{vp}} = 1.43 \times 10^{-7} \text{ m s}^{-2}$) (Fig. 2, solid lines).
204 Also, the velocity fields upstream (Fig. 2, Fig. 3) are very similar with $c = 10 \text{ kN m}^{-2}$ for MEB and its
205 correspondent mechanical parameters for VP. The maximum “southward” velocity upstream is reached
206 after approximately 15 h.

207 The effective ice thickness is generally similar for both rheologies (Fig. 3). In both cases, leads form
208 downstream of the channel and ridging occurs upstream of the channel. Some differences in the exact
209 location and shape of the leads and ridges are attributed to the different failure processes, namely the
210 damage propagation and the associated normal flow rule for the MEB and VP rheologies, respectively. For
211 instance, some ice remains attached to the islands downstream of the channel in the VP simulation as the
212 deformation transitions from lead opening downstream of the islands to pure shear on the sides, while in

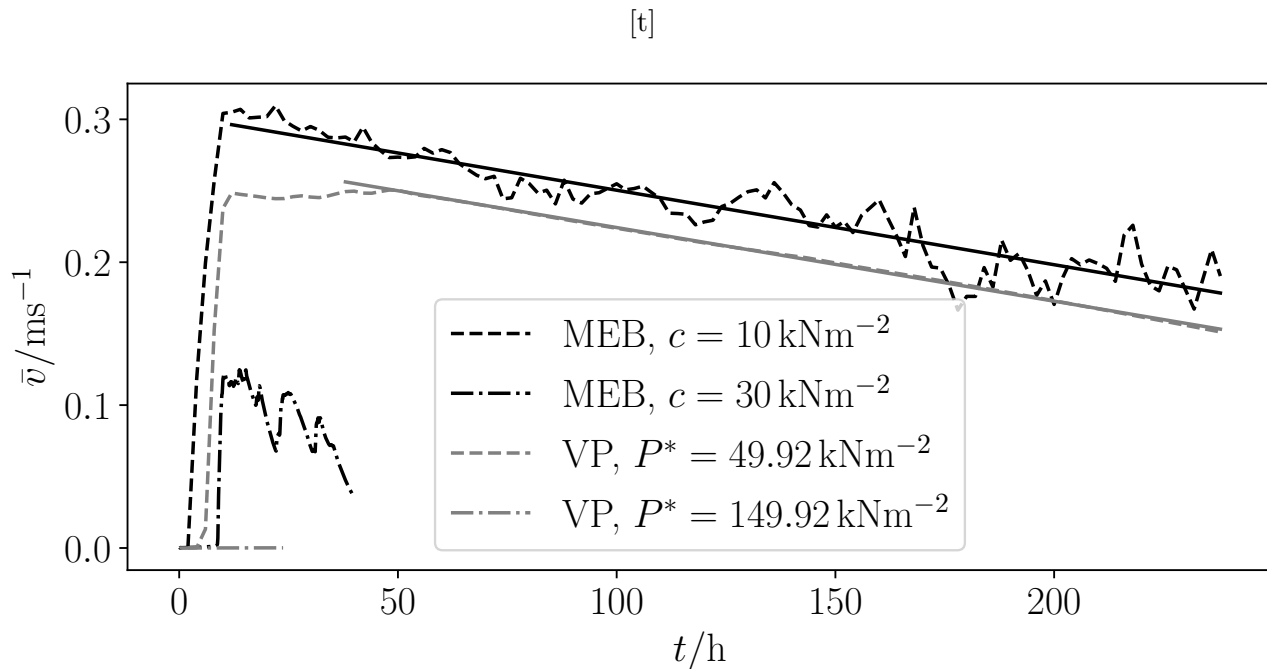


Fig. 2. Averaged ice velocities parallel to channel upstream of channel. The sea ice does not move at all (VP) or rapidly stops (MEB) for the high cohesion case ($c = 30 \text{ kN m}^{-2}$, $P^* = 149.92 \text{ kN m}^{-2}$, dash-dotted lines). There is a slow and very similar stopping effect by the formation of an ice arch in both the MEB simulation and the VP simulation for the low cohesion case ($c = 10 \text{ kN m}^{-2}$, $P^* = 49.92 \text{ kN m}^{-2}$, dashed lines). The solid lines are the linear regression of the ice velocities.

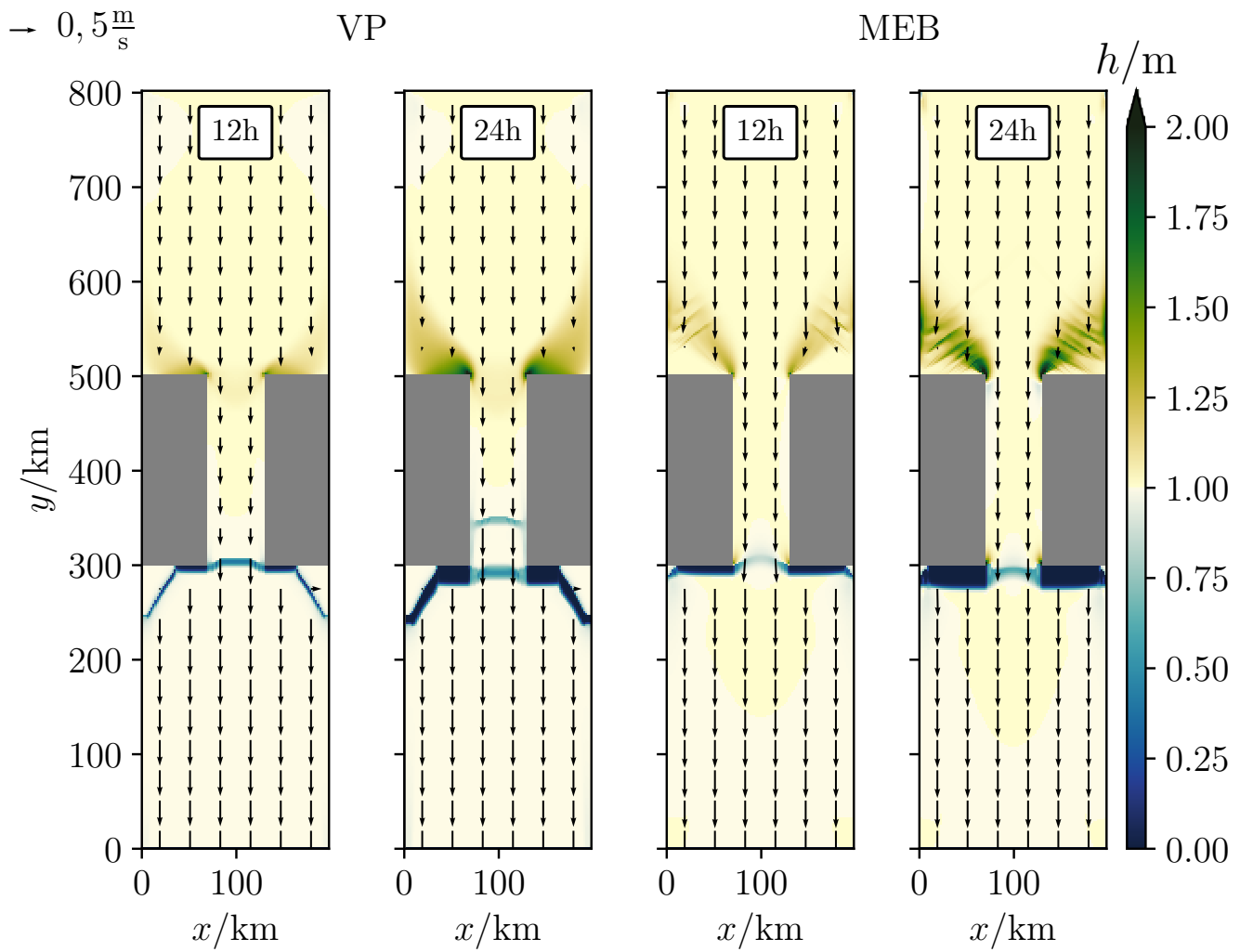


Fig. 3. Snapshots of the effective ice thickness h and the ice drift velocity (arrows) for the VP rheology (left two panels) and the MEB rheology (right two panels) at $t = 12\text{h}$ and 24h . Note that the colour scale is chosen to emphasize deviations from the initial state ($h = 1\text{ m}$).

213 the MEB simulation the damage propagation is directly along the coastlines. Upstream of the channel,
214 the ridging area contains additional diagonal patterns in the MEB simulations due to the formation of
215 secondary fracture lines, while the ice thickness is smoother and more uniform in the VP simulations.

216 Our results agree with other ice arch simulations (Dumont and others, 2009; Dansereau and others,
217 2017; Plante, 2021, Chapter 5) and demonstrate that the cohesive strength of the ice plays an important
218 role in ice arching so that corresponding mechanical parameters lead to similar results between the different
219 rheologies.

220 Quadratic domain with cyclonic winds

221 A quadratic box with closed boundaries, constant anticyclonic (clockwise) ocean circulation and a moving
222 cyclonic wind system was suggested to compare different sea ice models (Mehlmann and others, 2021).
223 This “benchmark” problem was used to analyse how different VP models simulate sea ice deformation,
224 in particular LKFs. Here, the “benchmark” problem is repeated with the MITgcm using different grid
225 spacings ($\Delta x = 2, 4, 8$ km) to analyse spatial heterogeneity in both the MEB and VP models. Note that
226 for all grid resolutions the simulation is produced with the same time step ($\Delta t = 120$ s for VP, $\Delta t = 0.5$ s
227 for MEB). In the MEB case, this value is chosen to ensure that the constitutive equation is well resolved
228 at the highest resolution (i.e., according to the CFL criterion for resolving the elastic waves).

229 To choose similar yield curve parameters for MEB and VP as in the channel experiment, we have to
230 consider the following: The VP-parameters of this benchmark $P^* = 27.5$ kN/m² with $e = 2$ and no tensile
231 stress ($k = 0$) lead to a very low cohesion of 1.56 kN m² (Eq. 6). Using the large P^* values implied by the
232 cohesion of the channel experiment in the VP rheology would change the benchmark dramatically from
233 previously published results (Mehlmann and others, 2021), so that to compare the different rheologies we
234 instead adjust the MEB parameters to match the low VP cohesion. The low cohesion of 1.56 kN m² leads
235 to very low stress states. For comparison, we also use a high value of $c = 25$ kN m². These cohesion values
236 cover the range of previously reported values (Plante and others, 2020; Dansereau and others, 2016). The
237 model parameters for the experiments are summarized in Table 1.

238 Results from Mehlmann and others (2021) are reproduced by our VP simulations, with more radial
239 features in the compressive stress field than circular ones and without tensile stress states (Fig. 4). In both
240 models, there are fewer identifiable deformation patterns and the deformation fields also become smoother
241 with decreasing resolution (not shown, see Chapter 8 in Bourgett, 2022).

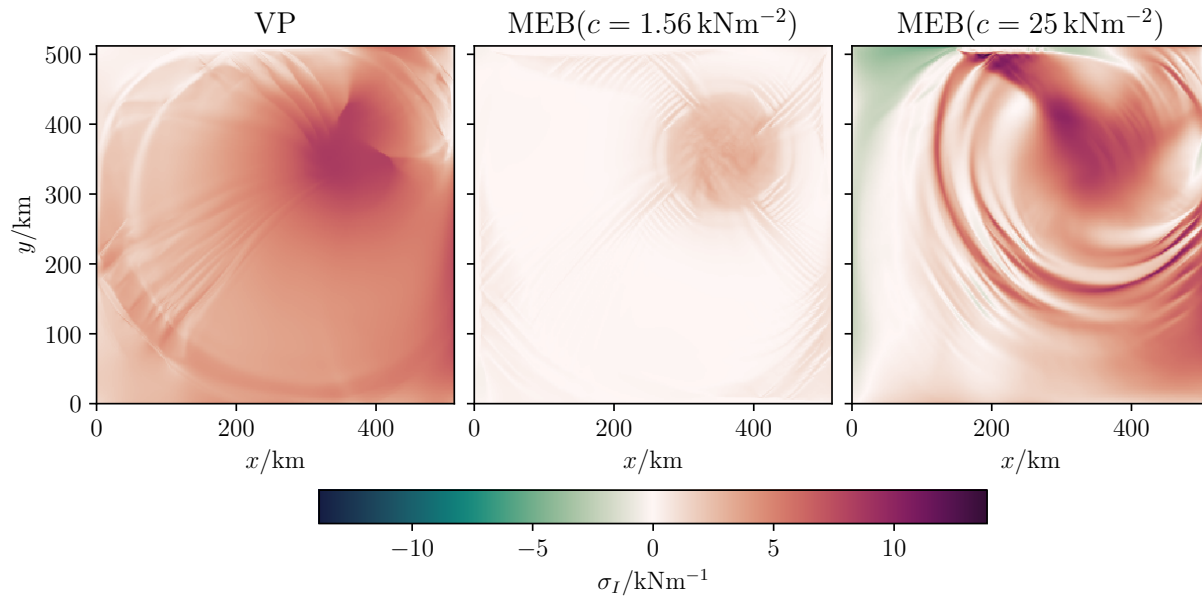


Fig. 4. Snapshot of the stress invariant σ_I at $t = 2$ d and with $\Delta x = 2$ km of the VP simulation on the left and the MEB rheology with low (center) and high (right) cohesion. Positive values mean convergence. Divergent (negative) stress state are only allowed in the MEB-model. The size of the stress invariant depends on the choice of the cohesion.

242 The presence of radial or circular features and the range of the stress values depends to some degree on
 243 the choice of cohesion for the MEB rheology. Using the MEB rheology with a cohesion similar to that of the
 244 VP simulations yields much smaller stresses but otherwise similar features as in the VP simulations, with
 245 mostly radial features and only a few circular stress features. Increasing the cohesion in the MEB model to
 246 get similar stress states as in the VP simulation (Fig. 4), however, changes these patterns and the features
 247 are mostly circular. Using the VP rheology with analogous values to match the cohesive stress states
 248 results in the same dependency (not shown). This dependency suggests that the shape of the features are
 249 sensitive to the shear strength; fewer cohesive stress states (gray area in Fig. 1) strongly result in smaller
 250 shear stresses, which favors radial features, while more cohesive stress states result in larger shear stresses,
 251 which favors the production of circular features.

252 There are other yield-curve related causes for the different stress fields: for example, the different yield
 253 curve shape of the MEB rheology allows isotropic tensile stresses (see negative σ_I in Fig. 4), while the VP
 254 rheology with the standard elliptical yield curve does not; and the MEB model does not have a flow rule.
 255 Neither of these causes are explored here.

256 Further, the rheologies are compared by means of the number of LKFs as detected by a tracking
 257 algorithm (Hutter and Losch, 2020, with parameter modifications by Mehlmann and others, 2021) (Table 2).

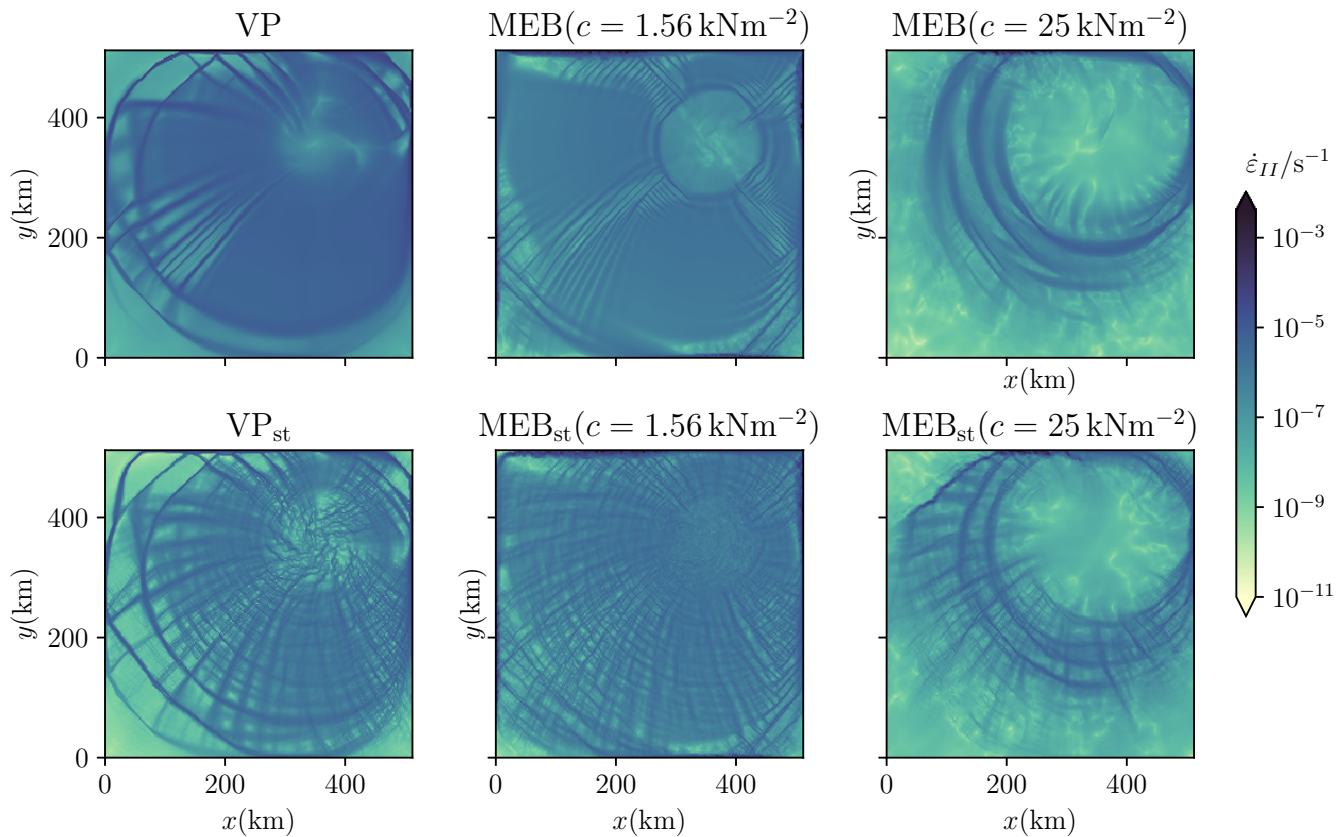


Fig. 5. Snapshots of the shear deformation rate $\dot{\epsilon}_{II}$ at $t = 2$ d and with $\Delta x = 2$ km of simulations without (above) and with (below) a stochastic parameterisation of the heterogeneity at the grid-scale (index “st”). The shear deformation rate using the VP rheology on the left and using the MEB rheology with low and high cohesion in the center and on the right.

258 The number of LKFs increases for both rheologies with increasing resolution. As expected because of the
 259 damage mechanism and long-range elastic interactions that produce sub-grid fracturing (Dansereau and
 260 others, 2016), the MEB simulation (independent of the choice of cohesion) has more LKFs than the VP
 261 simulation on all grids, especially on $\Delta x = 2$ km grid. Increasing the cohesion tends to lead to fewer LKFs
 262 (Table 2). Note that the decreased heterogeneity in the MEB simulations with high cohesion is associated
 263 with a much less extensive damage field. As the damage mechanism is known to be a numerical error
 264 integrator (Plante and Tremblay, 2021), this raises a question about the impact of numerical noise in
 265 seeding the heterogeneity.

Table 2. Number of LKFs for both VP and MEB rheology for simulations with 2 km, 4 km, and 8 km grid spacing Δx . The index “st” indicates that the simulation uses a stochastic parameterisation of c (cohesion) for the MEB rheology or P^* (ice strength) for the VP rheology. The MEB simulations are run with a high value of $c = 25 \text{ kN m}^2$ and with a low value of $c = 1.56 \text{ kN m}^2$

	Grid resolution Δx		
	2 km	4 km	8 km
MEB ($c = 25 \text{ kNm}^{-2}$)	128	51	21
MEB _{st} ($c = 25 \text{ kNm}^{-2}$)	241	76	23
MEB ($c = 1.56 \text{ kNm}^{-2}$)	143	52	15
MEB _{st} ($c = 1.56 \text{ kNm}^{-2}$)	390	89	21
VP	51	31	7
VP _{st}	317	106	30

266 STOCHASTIC PARAMETERISATION

267 One of the main motivations to develop a brittle rheology was the observation that models with VP rheology
 268 underestimate observed spatial heterogeneity (Girard and others, 2011). We indeed found the MEB solution
 269 to be more heterogeneous. Alternatively, heterogeneity can be increased with stochastic parameterisations
 270 (Juricke and others, 2013, their Fig. 6, and personal communication). In fact, early brittle models used
 271 a stochastic cohesion parameter c to introduce disorder (Girard and others, 2011; Dansereau and others,
 272 2017). We now adopt the same method to account for faults and cracks in the ice below the spatial grid
 273 scale Δx and draw the cohesion parameter c from a (pseudo-)random uniform distribution between $0.5c_0$
 274 and $1.5c_0$ of the unperturbed cohesion c_0 . The resulting heterogeneous cohesion field is constant in time
 275 throughout the simulation. Because the critical stresses σ_c and σ_t depend on c (Eqs. 3 and 4), a stochastic
 276 cohesion also leads to a different (but constant-in-time) damage criterion for each grid cell.

277 With the stochastic cohesion the number of LKFs increases for all grid resolutions independent of the
 278 cohesion (Table 2). The number of LKFs for the MEB simulations with the stochastic cohesion is also
 279 much higher than for the VP simulations discussed above (consistent with Girard and others, 2011).

280 Can we also obtain more spatial heterogeneity with stochastic parameters within the VP model? The
 281 VP model does not contain the fast feedback caused by the damage parameter, but the ice strength P^* can
 282 be perturbed by drawing from the same (pseudo-)random field as the cohesion in the MEB rheology, such

283 that the elliptic yield curve is enlarged or reduced for each grid cell according to $P^{*'} \in [0.5P^*, 1.5P^*]$. This
284 choice of P^* increases the number of LKFs in all resolutions (Table 2). The LKF numbers are comparable
285 to the corresponding MEB numbers and even higher for lower resolutions.

286 In both rheologies, heterogeneity of the results can be increased by introducing spatial variability to
287 mechanical ice properties (c , P^*). The simulations (e.g., shear deformation rate, Fig. 5) contain features
288 of heterogeneity that appear similar to previous results (Girard and others, 2011, their Fig. 3b). We find
289 (Table 2) that a VP model with a stochastic parameterisation can have a similar spatial heterogeneity as
290 the MEB rheology. Note, that here a random perturbation of mechanical parameters was similar in both
291 rheologies, whereas Girard and others (2011) compared a standard VP model with smooth ice strength to
292 an EB model with stochastic cohesion. We also note, that this random perturbation of cohesion is generally
293 not used in realistic large scale MEB or BBM simulations with realistic domains (e.g., Rampal and others,
294 2016; Ólason and others, 2022)

295 CONCLUSION

296 Simulations with the MEB rheology tend to be more heterogeneous (i.e., have more linear kinematic
297 features) than simulations with the standard VP rheology. This result was anticipated, but shown here
298 in a controlled environment without confounders. Furthermore, we demonstrate that adding disorder by
299 stochastic mechanical parameters (cohesion for MEB, ice strength for VP) increases heterogeneity to similar
300 levels in the VP and MEB simulations. We conclude that grid-scale heterogeneity is one important driver
301 to produce prominent large-scale deformation features, such as LKFs. Grid-scale heterogeneity can be
302 introduced in various ways, for example, by a brittle rheology based on physical considerations or by local
303 modification (physical or statistical) of material properties. The latter can be applied to sea ice models
304 independent of the constitutive equation.

305 By appropriate choice of model parameters, the most important material property (here: cohesion in
306 a landfast ice simulation in a channel) can be similar between MEB and VP rheologies. This choice leads
307 to similar deformation patterns (Fig. 5, left and middle column), but the stress states are very different in
308 magnitude between VP and MEB (Fig. 4, left and middle pane). In contrast, tuning the stress states to be of
309 similar order of magnitude (Fig. 4, left and right pane) leads to very different deformation patterns (Fig. 5,
310 left and right column). In this sense, our results suggest that described differences between deformation
311 patterns can be decreased by tuning the yield curves of the respective rheology.

312 As a technical note, there is some structural similarity between the constitutive equations for VP and
313 MEB such that after re-interpretation of some variables, a large part of the VP code can be used for the im-
314 plementation of the MEB rheology (Plante and others, 2020). The time-derivative term, however, increases
315 error memory in the system (Plante and Tremblay, 2021). Numerical details, such as averaging between
316 center and corner points of the C-grid, prove to be crucial for stability of the MEB implementation (see
317 also Brodeau and others, 2024). The new damage equation and in particular the elastic wave propagation
318 further pose strict constraints on the time step, so that a time splitting method for the MEB code should
319 be used (Ólason and others, 2022).

320 In our simulations, disorder introduced by noise (stochastic parameters) seems to be an important
321 driver of heterogeneity. The VP simulations without additional noise in the ice strength have much fewer
322 LKFs than those with a stochastic strength parameter. The same is true for the MEB simulations but to
323 a smaller extent. The damage parameter in MEB integrates failure by construction, but also numerical
324 errors (Plante and Tremblay, 2021). We speculate that these numerical errors may trigger failure and plan
325 to investigate if using a stabilizing scheme for stress correction that minimizes the numerical errors (Plante
326 and Tremblay, 2021) will also reduce the simulated heterogeneity.

327 REFERENCES

- 328 Berner J, Achatz U, Batte L, Bengtsson L, De La Camara A, Christensen HM, Colangeli M, Coleman DR, Crommelin
329 D, Dolaptchiev SI and others (2017) Stochastic parameterization: Toward a new view of weather and climate
330 models. *Bulletin of the American Meteorological Society*, **98**(3), 565–588
- 331 Bouchat A and Tremblay B (2017) Using sea-ice deformation fields to constrain the mechanical strength parameters
332 of geophysical sea ice. *Journal of Geophysical Research: Oceans*, **122**(7), 5802–5825
- 333 Bouchat A, Hutter NC, Dupont JCF, Dukhovskoy DS, Garric G, Lee YJ, Lemieux JF, Lique C, Losch M, Maslowski
334 W, Myers PG, Ólason E, Rampal P, Rasmussen T, Talandier C, Tremblay B and Wang Q (2022) Sea Ice Rheology
335 Experiment (SIREx), Part I: Scaling and statistical properties of sea-ice deformation fields. *J. Geophys. Res.*,
336 **127**(4), e2021JC017666 (doi: 10.1029/2021JC017667)
- 337 Bourgett M (2022) *Implementation of a Maxwell Elasto-Brittle Rheology in a Sea Ice Model Coupled*
338 *to an Ocean*. Master's thesis, TU Dortmund, Dortmund, GER, <http://hdl.handle.net/10013/epic.febd7a61-c2cf-4f4f-b86d-76beaf2d4378>
339

- 340 Boutin G, Ólason E, Rampal P, Regan H, Lique C, Talandier C, Brodeau L and Ricker R (2023) Arctic sea ice mass
341 balance in a new coupled ice–ocean model using a brittle rheology framework. *The Cryosphere*, **17**(2), 617–638
- 342 Brodeau L, Rampal P, Ólason E and Dansereau V (2024) Implementation of a brittle sea-ice rheology in an Eule-
343 rian, finite-difference, C-grid modeling framework: Impact on the simulated deformation of sea-ice in the Arctic.
344 *Geoscientific Model Development Discussions*, **2024**, 1–46 (doi: 10.5194/gmd-2023-231)
- 345 Danilov S, Sidorenko D, Wang Q and Jung T (2017) The Finite-volumE Sea ice–Ocean model (FESOM2). *Geosci-*
346 *entific Model Development*, **10**(2), 765–789
- 347 Dansereau V, Weiss J, Saramito P and Lattes P (2016) A Maxwell elasto-brittle rheology for sea ice modelling. *The*
348 *Cryosphere*, **10**(3), 1339–1359
- 349 Dansereau V, Weiss J, Saramito P, Lattes P and Coche E (2017) Ice bridges and ridges in the Maxwell-EB sea ice
350 rheology. *The Cryosphere*, **11**(5), 2033–2058
- 351 Dumont D, Gratton Y and Arbetter TE (2009) Modeling the dynamics of the North Water polynya ice bridge.
352 *Journal of Physical Oceanography*, **39**(6), 1448–1461
- 353 Girard L, Bouillon S, Weiss J, Amitrano D, Fichfet T and Legat V (2011) A new modeling framework for sea-ice
354 mechanics based on elasto-brittle rheology. *Annals of Glaciology*, **52**(57), 123–132
- 355 Hibler W, Hutchings J and Ip C (2006) Sea-ice arching and multiple flow states of Arctic pack ice. *Annals of*
356 *Glaciology*, **44**, 339–344
- 357 Hibler WD III (1979) A dynamic thermodynamic sea ice model. *J. Phys. Oceanogr.*, **9**(4), 815–846
- 358 Hunke EC and Dukowicz JK (1997) An elastic–viscous–plastic model for sea ice dynamics. *Journal of Physical*
359 *Oceanography*, **27**(9), 1849–1867
- 360 Hutter N and Losch M (2020) Feature-based comparison of sea ice deformation in lead-permitting sea ice simulations.
361 *The Cryosphere*, **14**(1), 93–113
- 362 Hutter NC, Bouchat A, Dupont F, Dukhovskoy DS, Koldunov NV, Lee YJ, Lemieux JF, Lique C, Losch M, Maslowski
363 W, Myers PG, Ólason E, Rampal P, Rasmussen T, Talandier C, Tremblay B and Wang Q (2022) Sea Ice Rheology
364 Experiment (SIREx), Part II: Evaluating simulated linear kinematic features in high-resolution sea-ice simulations.
365 *J. Geophys. Res.*, **127**(4), e2021JC017666 (doi: 10.1029/2021JC017666)
- 366 Ip CF (1993) *Numerical investigation of different rheologies on sea-ice dynamics*. Dartmouth College
- 367 Juricke S, Lemke P, Timmermann R and Rackow T (2013) Effects of stochastic ice strength perturbation on Arctic
368 finite element sea ice modeling. *Journal of climate*, **26**(11), 3785–3802

- 369 Kimmritz M, Danilov S and Losch M (2016) The adaptive EVP method for solving the sea ice momentum equation.
370 *Ocean Modelling*, **101**, 59–67
- 371 König Beatty C and Holland DM (2010) Modeling landfast sea ice by adding tensile strength. *J. Phys. Oceanogr.*,
372 **40**(1), 185–198 (doi: 10.1175/2009JPO4105.1)
- 373 Kubat I, Sayed M, Savage S and Carrieres T (2006) Flow of ice through converging channels. *International Journal*
374 *of Offshore and Polar Engineering*, **16**(04)
- 375 Lemieux JF, Tremblay B, Thomas S, Sedláček J and Mysak LA (2008) Using the preconditioned Generalized Mini-
376 mum RESidual (GMRES) method to solve the sea-ice momentum equation. *J. Geophys. Res.*, **113**(C10004) (doi:
377 10.1029/2007JC004680)
- 378 Lemieux JF, Tremblay B, Sedláček J, Tupper P, Thomas S, Huard D and Auclair JP (2010) Improving the numerical
379 convergence of viscous-plastic sea ice models with the Jacobian-free Newton-Krylov method. *J. Comp. Phys.*, **229**,
380 2840–2852 (doi: 10.1016/j.jcp.2009.12.011c)
- 381 Lemieux JF, Dupont F, Blain P, Roy F, Smith GC and Flato GM (2016) Improving the simulation of landfast ice by
382 combining tensile strength and a parameterization for grounded ridges. *Journal of Geophysical Research: Oceans*,
383 **121**(10), 7354–7368
- 384 Losch M and Danilov S (2012) On solving the momentum equations of dynamic sea ice models with implicit solvers
385 and the Elastic Viscous-Plastic technique. *Ocean Modelling*, **41**, 42–52 (doi: 10.1016/j.ocemod.2011.10.002)
- 386 Losch M, Menemenlis D, Campin JM, Heimbach P and Hill C (2010) On the formulation of sea-ice models. part 1:
387 Effects of different solver implementations and parameterizations. *Ocean Modelling*, **33**(1-2), 129–144
- 388 Losch M, Fuchs A, Lemieux JF and Vanselow A (2014) A parallel Jacobian-free Newton-Krylov solver for a coupled
389 sea ice-ocean model. *J. Comp. Phys.*, **257**(A), 901–910, ISSN 0021-9991 (doi: 10.1016/j.jcp.2013.09.026)
- 390 Marshall J, Adcroft A, Hill C, Perelman L and Heisey C (1997) A finite-volume, incompressible Navier Stokes model
391 for studies of the ocean on parallel computers. *J. Geophys. Res.*, **102**(C3), 5753–5766 (doi: 10.1029/96JC02775)
- 392 Mehlmann C, Danilov S, Losch M, Lemieux JF, Hutter N, Richter T, Blain P, Hunke E and Korn P (2021) Simulating
393 linear kinematic features in viscous-plastic sea ice models on quadrilateral and triangular grids with different
394 variable staggering. *Journal of Advances in Modeling Earth Systems*, **13**(11), e2021MS002523
- 395 MITgcm Group (2021) MITgcm User Manual. Online documentation, MIT/EAPS, Cambridge, MA 02139, USA (doi:
396 10.5281/zenodo.1409237), <https://mitgcm.readthedocs.io/en/latest>

- 397 Ólason E, Boutin G, Korosov A, Rampal P, Williams T, Kimmritz M, Dansereau V and Samaké A (2022) A new
398 brittle rheology and numerical framework for large-scale sea-ice models. *Journal of Advances in Modeling Earth*
399 *Systems*, **14**(8), e2021MS002685
- 400 Plante M (2021) *A generalized damage parameterization within the Maxwell Elasto-Brittle rheology: ap-*
401 *plications to ice fractures and ice arches in landfast ice simulations*. Phd thesis, McGill University,
402 <https://escholarship.mcgill.ca/concern/theses/gf06g703w>
- 403 Plante M and Tremblay LB (2021) A generalized stress correction scheme for the Maxwell elasto-brittle rheology:
404 impact on the fracture angles and deformations. *The Cryosphere*, **15**(12), 5623–5638
- 405 Plante M, Tremblay LB, Losch M and Lemieux JF (2020) Landfast sea ice material properties derived from ice bridge
406 simulations using the Maxwell elasto-brittle rheology. *The Cryosphere*, **14**(6), 2137–2157
- 407 Rampal P, Bouillon S, Ólason E and Morlighem M (2016) neXtSIM: a new Lagrangian sea ice model. *The Cryosphere*,
408 **10**(3), 1055–1073
- 409 Ringeisen D, Losch M, Tremblay LB and Hutter N (2019) Simulating intersection angles between conjugate faults in
410 sea ice with different viscous–plastic rheologies. *The Cryosphere*, **13**(4), 1167–1186
- 411 Ringeisen D, Tremblay LB and Losch M (2021) Non-normal flow rules affect fracture angles in sea ice viscous–plastic
412 rheologies. *The Cryosphere*, **15**(6), 2873–2888
- 413 Ringeisen D, Losch M and Tremblay LB (2023) Teardrop and parabolic lens yield curves for viscous-plastic sea ice
414 models: New constitutive equations and failure angles. *Journal of Advances in Modeling Earth Systems*, **15**(9),
415 e2023MS003613 (doi: <https://doi.org/10.1029/2023MS003613>)
- 416 Sodhi DS (1977) Ice arching and the drift of pack ice through restricted channels. Technical Report 77–18, Department
417 of Defense, Department of the Army, Corps of Engineers, Cold Regions Research and Engineering Laboratory,
418 Hanover, New Hampshire
- 419 Turner AK, Lipscomb WH, Hunke EC, Jacobsen DW, Jeffery N, Engwirda D, Ringler TD and Wolfe JD (2022)
420 MPAS-Seaice (v1.0.0): sea-ice dynamics on unstructured Voronoi meshes. *Geoscientific Model Development*, **15**(9),
421 3721–3751 (doi: [10.5194/gmd-15-3721-2022](https://doi.org/10.5194/gmd-15-3721-2022))
- 422 Walker D (1966) An approximate theory for pressures and arching in hoppers. *Chemical Engineering Science*, **21**(11),
423 975–997
- 424 Weiss J, Schulson EM and Stern HL (2007) Sea ice rheology from in-situ, satellite and laboratory observations:
425 Fracture and friction. *Earth and Planetary Science Letters*, **255**(1-2), 1–8